American Mineralogist, Volume 104, pages 1336–1344, 2019

Nixonite, $Na_2Ti_6O_{13}$, a new mineral from a metasomatized mantle garnet pyroxenite from the western Rae Craton, Darby kimberlite field, Canada

Chiara Anzolini[1,*], Fei Wang[2], Garrett A. Harris[1], Andrew J. Locock[1], Dongzhou Zhang[3], Fabrizio Nestola[4], Luca Peruzzo[5], Steven D. Jacobsen[2], and D. Graham Pearson[1]

[1]Department of Earth and Atmospheric Sciences, 1-26 Earth Sciences Building, University of Alberta, Edmonton, Alberta T6G 2E3, Canada
[2]Department of Earth and Planetary Sciences, Northwestern University, Evanston, Illinois 60208, U.S.A.
[3]School of Ocean and Earth Science and Technology, Hawai'i Institute of Geophysics and Planetology, University of Hawaii at Manoa, Honolulu, Hawaii 966822, U.S.A. Orcid 0000-0002-6679-892X
[4]Department of Geosciences, University of Padova, Via G. Gradenigo 6, 35131 Padova, Italy. Orcid 0000-0002-4875-5125
[5]CNR, Istituto di Geoscienze e Georisorse, Sezione di Padova, Via G. Gradenigo 6, 35131 Padova, Italy

Abstract

Nixonite (IMA 2018-133), ideally $Na_2Ti_6O_{13}$, is a new mineral found within a heavily metasomatized pyroxenite xenolith from the Darby kimberlite field, beneath the west-central Rae Craton, Canada. It occurs as microcrystalline aggregates, 15 to 40 μm in length. Nixonite is isostructural with jeppeite, $K_2Ti_6O_{13}$, with a structure consisting of edge- and corner-shared titanium-centered octahedra that enclose alkali-metal ions. The Mohs hardness is estimated to be between 5 and 6 by comparison to jeppeite, and the calculated density is 3.51(1) g/cm^3. Electron microprobe wavelength-dispersive spectroscopic analysis (average of 6 points) yielded: Na_2O 6.87, K_2O 5.67, CaO 0.57, TiO_2 84.99, V_2O_3 0.31, Cr_2O_3 0.04, MnO 0.01, Fe_2O_3 0.26, SrO 0.07, total 98.79 wt%. The empirical formula, based on 13 O atoms, is: $(Na_{1.24}K_{0.67}Ca_{0.06})_{\Sigma 1.97}(Ti_{5.96}V_{0.023}Fe_{0.018})_{\Sigma 6.00}O_{13}$ with minor amounts of Cr and Mn. Nixonite is monoclinic, space group *C*2/*m*, with unit-cell parameters a = 15.3632(26) Å, b = 3.7782(7) Å, c = 9.1266(15) Å, β = 99.35(15)°, and V = 522.72(1) Å^3, Z = 2. Based on the average of seven integrated multi-grain diffraction images, the strongest diffraction lines are [d_{obs} in Å (I in %) (*hkl*)]: 3.02 (100) (310), 3.66 (75) (110), 7.57 (73) (200), 6.31 (68) ($20\bar{1}$), 2.96 (63) ($31\bar{1}$), 2.96 (63) ($20\bar{3}$), and 2.71 (62) (402). The five main Raman peaks of nixonite, in order of decreasing intensity, are at 863, 280, 664, 135, and 113 cm^{-1}. Nixonite is named after Peter H. Nixon, a renowned scientist in the field of kimberlites and mantle xenoliths. Nixonite occurs within a pyroxenite xenolith in a kimberlite, in association with rutile, priderite, perovskite, freudenbergite, and ilmenite. This complex Na-K-Ti-rich metasomatic mineral assemblage may have been produced by a fractionated Na-rich kimberlitic melt that infiltrated a mantle-derived garnet pyroxenite and reacted with rutile during kimberlite crystallization.

Keywords: Nixonite, new mineral, crystal structure, jeppeite, mantle xenolith, kimberlite, Rae Craton

Introduction

The Darby kimberlite field, located ~200 km southwest of the community of Kugaaruk, Nunavut, Canada, provides an opportunity to study mantle xenoliths from beneath the western portion of the central Rae Craton. To date, the Darby kimberlite field contains nine bodies, of which eight are kimberlitic (Counts 2007, http://www.24hgold.com/english/news-company-gold-silver-darby-project-continues-to-produce-diamondiferous-kimberlites.aspx?articleid=200573). The kimberlite eruption age is estimated from a Rb-Sr isochron to be 542.2 ± 2.6 Ma (Harris et al. 2018). Further details about lithosphere depletion, the mantle geotherm and crustal/lithosphere thickness across the Rae Craton are found in Harris et al. (2018), which provides compositional and geochronological information on mantle xenoliths and kimberlite-derived mineral concentrates from the Darby kimberlite field.

Six garnet pyroxenites erupted by the Darby kimberlites and studied in detail by Harris et al. (2018) contain various rare Ti-rich minerals, including jeppeite, $K_2Ti_6O_{13}$, as discrete grains or reaction rims on rutile. In particular, one mantle-derived, plagioclase-free garnet pyroxenite xenolith, sample M-2B-3A, contains rutile with a complex reaction rim (Supplemental[1] Fig. S1) comprised of priderite [$K(Ti,Fe)_8O_{16}$], perovskite ($CaTiO_3$), freudenbergite [$Na_2(Ti,Fe)_8O_{16}$], ilmenite ($FeTiO_3$), and nixonite ($Na_2Ti_6O_{13}$) (Fig. 1). Nixonite is the first natural occurrence of $Na_2Ti_6O_{13}$ and is the Na-rich analog of jeppeite, which occurs as a groundmass mineral in lamproites (Pryce et al. 1984; Grey et al. 1998; Jaques 2016). Previously, $Na_2Ti_6O_{13}$ was only known as a synthetic material (Andersson and Wadsley 1962) and has been suggested for potential use in batteries (e.g., Cech et al. 2017).

Here we describe the new mineral nixonite in terms of its physical, chemical, optical, and structural properties, and suggest a possible mechanism of formation. Nixonite is named after Peter H. Nixon (b. 1935), who was Professor of Mantle Geology at Leeds University, U.K., and is now retired. In addition to a lifetime of work on kimberlites and their mantle- and deep crustal-derived xenoliths, he named knorringite, the high-Cr garnet end-member with the formula $Mg_3Cr_2(SiO_4)_3$ (Nixon and Hornung 1968). Nixon also discovered the Letseng kim-

* E-mail: anzolini@ualberta.ca; Orcid 0000-0001-8166-9416

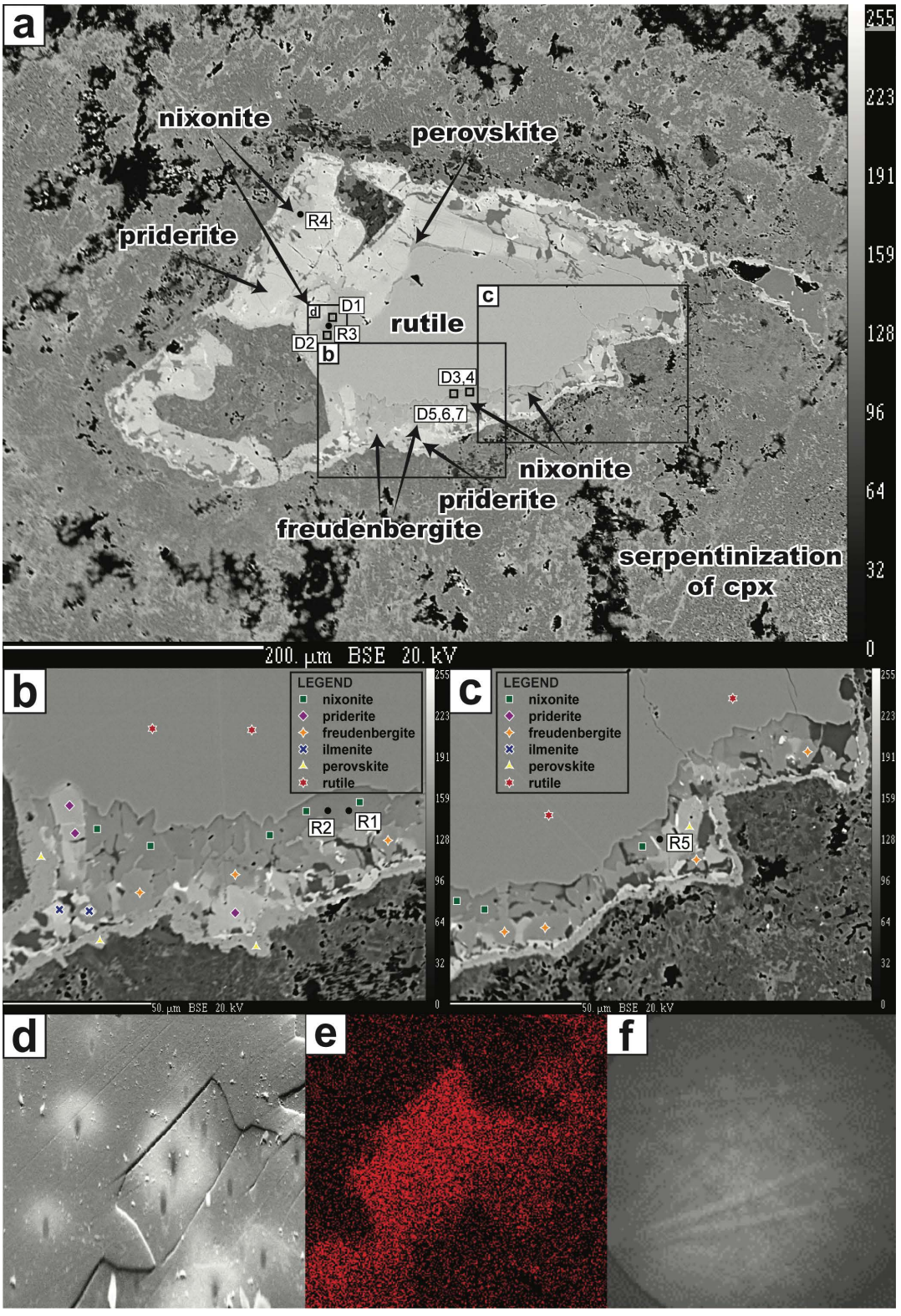

FIGURE 1. (**a**) Backscattered image of rutile grain with complex reaction rim containing nixonite (in five locations), priderite, freudenbergite, ilmenite, and perovskite; (**b** and **c**) portions of the rutile grain; (**d**) nixonite area in which (**e**) a Na EDS map and (**f**) an EBSD pattern were collected. The EBSD pattern acquired from the Na-rich area was indexed in the same crystal system as jeppeite, confirming that nixonite is the Na-dominant form of jeppeite. Black dots and black squares indicate where Raman spectra and diffraction patterns were collected, respectively. (Color online.)

berlite during his Ph.D., now a world-famous source of large high-quality diamonds, and described the second occurrence of yimengite (Nixon and Condliffe 1989), a potassium-chromium oxide of the magnetoplumbite group that occurs in the mantle as a metasomatic mineral. Peter Nixon was a visionary who brought the scientific community's attention to the growing evidence of orogenically emplaced mantle rocks from the diamond stability field, providing the first strong evidence for this process in the form of graphitized diamonds from the Beni Bousera peridotite massif (Pearson et al. 1989). Nixonite has been approved by the Commission on New Minerals, Nomenclature and Classification with the code IMA 2018-133, and the holotype material is deposited at the Royal Ontario Museum (Canada), under catalog number M59224.

Experimental methods

Scanning electron microscopy–energy-dispersive spectroscopy

To verify the distribution of Na over the nixonite area (Fig. 1e), we used a CamScan MX3000 electron microscope equipped with a LaB_6 source, a four-quadrant solid-state backscattered-electron detector and an EDAX EDS system for micro-analysis installed at the Department of Geosciences of the University of Padova. The measurement conditions were: accelerating voltage, 20 kV; filament emission, ~13 nA; working distance, 27 mm.

The EBSD pattern (Fig. 1f) collected on this same area was indexed in the same crystal system as jeppeite, confirming that the nixonite grain was the Na-dominant analog of jeppeite. EBSD analyses were performed at CNR-ICMATE in Padova, using a Quanta 200F FEG-ESEM system operating in high-vacuum mode with an accelerating voltage of 30 kV, emission current of 174 μA and beam spot of 4.5 μm, without any conductive coating. EBSD patterns were collected at a working distance of 10 mm and a specimen tilt of 75° using an EDAX DigiView EBSD system. The instrument was controlled by the OIMTM 5.31 software, which contains a large EBSD pattern database.

Electron probe microanalysis

Nixonite was analyzed by electron probe microanalysis (EPMA) on a CAMECA SX100 instrument at the Department of Earth and Atmospheric Sciences, University of Alberta. The analyses were conducted using wavelength-dispersive spectroscopy (WDS) and an accelerating voltage of 20 kV, probe current of 20 nA, and a fully focused beam (<1 μm) for the oxides SiO_2, TiO_2, Al_2O_3, V_2O_3, Cr_2O_3, MnO, Fe_2O_3, MgO, CaO, Na_2O, K_2O, SrO, Nb_2O_5, and BaO. The precision for the major elements is better than 1%. Lower limits of detection were calculated in the Probe for EPMA software (Donovan et al. 2015) at the 99% confidence limit to be (in parts per million, rounded to the nearest 10, or 100 ppm for Ba): Nb 360, Si 80, Ti 180, Al 80, V 160, Cr 190, Fe 110, Mn 110, Mg 90, Ca 60, Sr 280, Ba 1200, Na 150, K 80. The elements Mg, Al, Si, Nb, and Ba were not found above the limits of detection. Oxide abundances and standards used for the elements above the limit of detection are listed in Table 1.

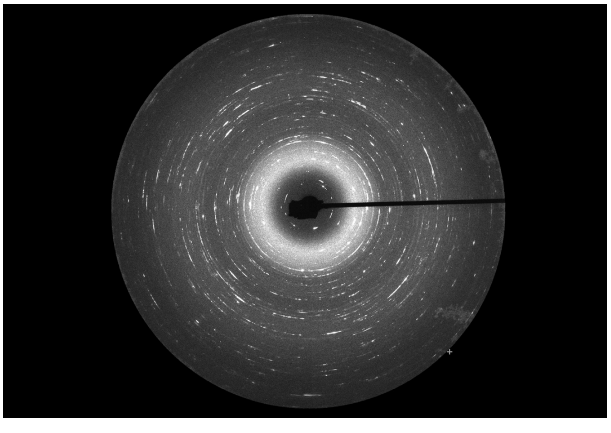

Figure 2. Example 2D X-ray diffraction image of nixonite collected at spot D2 in Figure 1 and corresponding to diffraction pattern DB2 in Figure 4. The diffraction pattern was collected with monochromatic synchrotron radiation (λ = 0.434 Å) focused to a spot size of 20 μm (vertical) by 15 μm (horizontal) at beamline 13-BMC (GSECARS) of the Advanced Photon Source, Argonne National Lab. The spotty nature of the 2D diffraction pattern in this configuration suggests the nixonite grain size is on the order of 1–2 μm.

Synchrotron X-ray diffraction

No single-crystal diffraction study was possible because of the microcrystalline nature of nixonite (Fig. 2) coupled with the fact that the sample is in a thick section embedded in resin, mounted on a glass slide. Unfortunately, this remains the only example of nixonite available for study. The sample was characterized by angle-dispersive synchrotron X-ray diffraction carried out at beamline GSECARS 13-BM-C of the Advanced Photon Source (APS), Argonne National Laboratory. The X-ray beam was monochromated with a silicon (311) crystal to a wavelength of 0.434 Å (28.6 keV) with 1 eV energy bandwidth. A Kirkpatrick-Baez mirror system was used to focus the beam to 20 μm (vertical) × 5 μm (horizontal) in full-width at half maximum at the sample position. A MAR165 charge-coupled device (CCD) detector (Rayonix) was used to collect the diffraction patterns. A NIST LaB_6 powder standard was used to calibrate the sample-detector distance and tilting angle (Zhang et al. 2017).

Micro-Raman spectroscopy and laser-stimulated fluorescence

Micro-Raman and fluorescence spectroscopy measurements were carried out at the Department of Earth and Planetary Sciences, Northwestern University, using a custom-built confocal optical system consisting of an Olympus BX microscope with 100× Mitutoyo M Plan Apo long working distance objective (numerical aperture 0.7, working distance 6.0 mm), focused into an Andor Shamrock 303i spectrograph (30 cm focal length) with Andor Newton DU970 CCD camera cooled to 188 K. For both Raman and fluorescence measurements, a 458 nm solid-state diode laser with 250 mW output was used as the excitation source (Melles Griot model BLS 85–601). A neutral-density filter was used to reduce the laser-power at the sample to ~6 mW. Raman spectra were recorded for 10 s, averaged over six accumulations from 0–4000 cm^{-1} shift using a holographic 1800 l/mm grating. Laser-stimulated fluorescence spectra were collected from 450–1100 nm using a 300 l/mm grating. The black dots in Figure 1, labeled R1 through R5, show where the Raman spectra were collected. Fluorescence spectra were recorded at spot R2.

Results

Appearance, physical, and optical properties

Nixonite occurs as aggregates, between 15 to 40 μm in length (Fig. 1), of microcrystalline grains whose domain size is not more than a few micrometers, based on the spotty diffraction rings that were observed in 2D synchrotron X-ray diffraction patterns collected with a 15 × 20 μm focused beam (Fig. 2). This micro-domain size prevented the determination of color, streak, cleavage, parting, tenacity, and fracture prop-

Table 1. WDS chemical analyses (wt%) carried out on nixonite and based on the average of six analysis points

Oxide	wt%	St.dev.	Range	Probe standard
Na_2O	6.87	0.68	5.93–7.60	$NaAlSi_3O_8$ 131705
K_2O	5.67	1.25	4.11–7.33	$KAlSi_3O_8$ Itrongay
CaO	0.57	0.36	0.30–1.26	$CaMgSi_2O_6$ Wakefield
TiO_2	84.99	0.50	84.08–85.34	TiO_2 MTI
V_2O_3	0.31	0.08	0.15–0.39	V Alfa
Cr_2O_3	0.04	0.03	0–0.07	Cr_2O_3 Alfa
MnO	0.01	0.01	0–0.02	$(Mn,Fe)_3Al_2Si_3O_{12}$ Navegadora Mine
Fe_2O_3	0.26	0.08	0.17–0.37	$FeTiO_3$ 96189
SrO	0.07	0.03	0.04–0.11	$SrTiO_3$ MTI
Total	98.79	0.70	97.55–99.57	

Note: Data have been rounded to the nearest 0.01 wt% oxide.

erties. However, we can assume the cleavage and tenacity to be similar to those of the K-analog jeppeite, which is brittle and cleaves along the (100) plane. No luster was observed but probably it is submetallic based on the analogy with jeppeite and the assumed mean refractive index (see below).

Although the density of nixonite was not measured because of the small size of the mineral grains, the density was calculated to be 3.51(1) g/cm^3, based on the unit-cell volume determined by X-ray diffraction and the chemical composition determined by electron probe microanalysis. The hardness was not determined because of the character of the material available. However, nixonite is the Na-analog of jeppeite, ideally $K_2Ti_6O_{13}$, which has a hardness between 5 and 6 on the Mohs scale. As synthetic $K_2Ti_6O_{13}$ has a density of 3.56 g/cm^3 (Cid-Dresdner and Buerger 1962) and nixonite has a calculated density of 3.51(1) g/cm^3, it is reasonable to expect that they have similar hardness. The micro-hardness could not be measured because of the very fine (~1 μm) grain size and a very limited amount of sample, precluding destructive measurements. Instead, we sought to maximize the amount of archived material.

The small crystal size and finely intergrown texture also prevented the measurement of the optical properties of nixonite. However, the optical properties of its K-analog, jeppeite, can provide guidance as to the mean refractive index of nixonite based on the compatibility index (Mandarino 1979, 1981). Jeppeite has α, β, and γ refractive indices of 2.13, 2.21, and 2.35, respectively, with average refractive index: $[(\alpha+\beta+\gamma)/3] = 2.23$ (Pryce et al. 1984). Nixonite should have an average refractive index in the same range as that of jeppeite, based on the similarity of the densities of their synthetic end-members ($Na_2Ti_6O_{13}$ has density d = 3.51 g/cm^3 and $K_2Ti_6O_{13}$ has density d = 3.56 g/cm^3). Alternatively, the average refractive index of nixonite can be computed (using the Gladstone-Dale constants together with its composition and calculated density) to be 2.27, which is very similar to the assumed value of 2.23 above. Calculation of the Gladstone-Dale relationship yields a compatibility index, $1 - (K_P/K_C) = 0.03$, rated as "excellent" (Mandarino 1981).

Chemical composition

The empirical formula of nixonite, calculated from the EPMA data in Table 1, on the basis of 13 O atoms per formula unit (apfu) is: $[Na_{1.24}K_{0.67}Ca_{0.06}]_{\Sigma 1.97}[Ti_{5.96}V_{0.023}Fe_{0.018}]_{\Sigma 6.00}O_{13}$, with minor amounts of Cr and Mn.

The simplified formula is $(Na,K)_2Ti_6O_{13}$, and the ideal formula is $Na_2Ti_6O_{13}$, which requires Na_2O 11.45 wt% and TiO_2 88.55 wt%. Elemental maps for K, Na, Ti, Ca, and Fe were acquired to outline zones of interest for characterization by X-ray diffraction (Figs. 1e and 3; Supplemental[1] Fig. S2). The nixonite and freudenbergite reaction rim are clearly shown by the Na elemental abundance map (Fig. 3b).

X-ray crystallography

The black squares in Figure 1, labeled D1 through D7, show where the multi-grain diffraction patterns were collected. As a result of the small grain size and the sample having to be measured in a thick section—with the likelihood of additional phases underlying the nixonite grains—multiple phases (mostly rutile and priderite) were observed along with the nixonite diffraction pattern (Fig. 4). Our procedure for dealing with multi-grain, multi-phase diffraction data is outlined below to extract crystallographic data for nixonite.

We first masked out rutile and priderite diffraction signals from the raw diffraction image, and then the masked diffraction image was integrated with the DIOPTAS software (Prescher and Prakapenka 2015). Individual peak positions (d-spacings are reported in Table 2) were fitted with the Gaussian peak shapes from the integrated diffraction pattern, and the UnitCell program (Holland and Redfern 1997) was used to determine unit-cell parameters (Fig. 5). Rietveld refinement was carried out on the pseudo-powder diffraction patterns generated by averaging seven integrated multi-grain diffraction patterns using the GSAS program (Toby and Von Dreele 2013). Our starting model of nixonite was revised from the $Na_2Ti_6O_{13}$ structure determined by Andersson and Wadsley (1962) with space group $C2/m$ on a synthetic material. In the Rietveld refinement, the cell parameters from UnitCell were fixed, whereas the atomic coordinates of

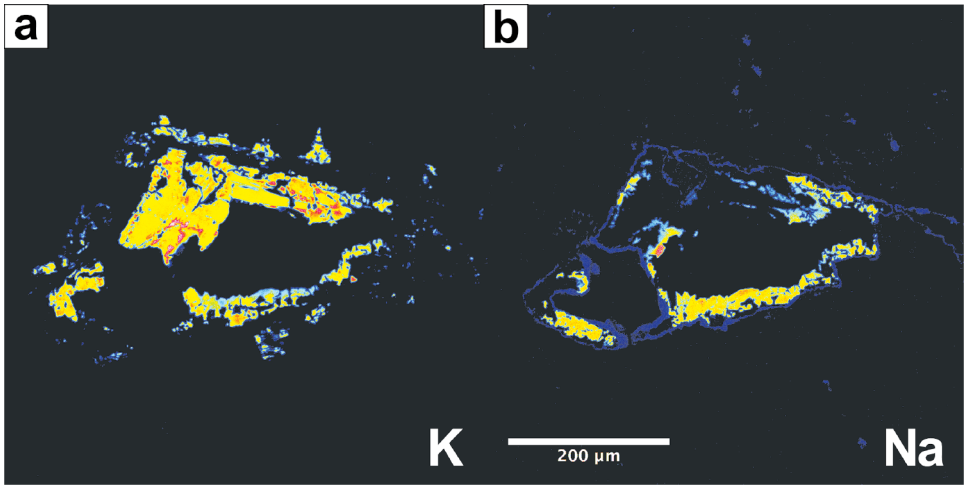

Figure 3. False-color (16 shades) X-ray intensity maps. (**a**) K map showing priderite, nixonite, and freudenbergite. (**b**) Na map displaying nixonite and freudenbergite in the reaction rim. Dark red shows the zone where nixonite is the most abundant. (Color online.)

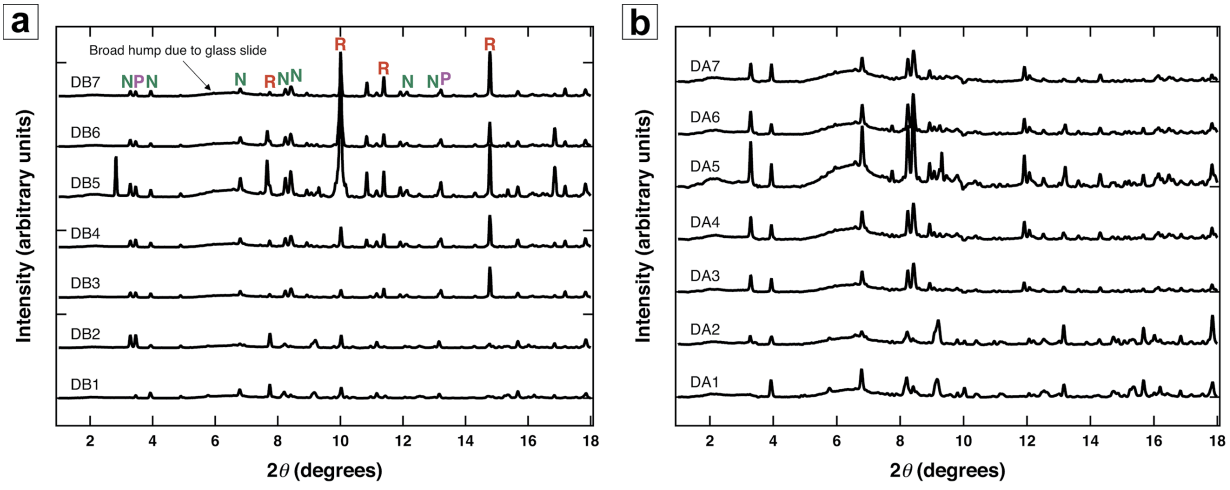

FIGURE 4. (**a**) X-ray diffraction patterns of nixonite at positions D1-D7, shown in Figure 1, before background correction and subtraction of other phases (N = nixonite, P = priderite, R = rutile). (**b**) X-ray diffraction patterns of nixonite at positions D1–D7, shown in Figure 1, after background correction and subtraction of other phases. (Color online.)

the (Na,K) position and the three Ti positions were refined (the atomic coordinates of the oxygen positions were not refined). Our diffraction data are consistent with the previously published structure models for synthetic $Na_2Ti_6O_{13}$ (Andersson and Wadsley 1962) and $K_2Ti_6O_{13}$ (Cid-Dresdner and Buerger 1962), although the R-factor for the model is ~57% due to poorly constrained intensities from the microcrystalline diffraction patterns. The refined unit-cell parameters are: $a = 15.3632(26)$ Å, $b = 3.7782(7)$ Å, $c = 9.1266(15)$ Å, $\beta = 99.35(15)°$, and $V = 522.72(1)$ Å^3 ($Z = 2$). The a:b:c ratio calculated from unit-cell parameters is 4.0663:1:2.4155. For a comparison of nixonite with synthetic $Na_2Ti_6O_{13}$ and other related species see Supplemental[1] Table S2.

TABLE 2. List of *d*-spacings (in angstroms), relative intensities, and *hkl* indices for nixonite obtained by pseudo-powder XRD, obtained by averaging seven "multi-grain" 2D diffraction patterns (see Fig. 2)

No.	I_{obs}	d_{obs} (Å)	I_{calc}	d_{calc} (Å)	h	k	l
1	73	7.57	100	7.58	2	0	0
2	68	6.31	67	6.33	2	0	1
3	4	4.18	4	4.18	2	0	2
4	8	3.77	2	3.79	4	0	0
5	75	3.66	80	3.67	1	1	0
6	5	3.34	1	3.35	1	1	1
7	7	3.28	2	3.31	4	0	1
8	100	3.02	79	3.03	3	1	0
9	63	2.96	65	2.96	3	1	1
10	63	2.96	44	2.96	2	0	3
11	39	2.79	17	2.79	1	1	2
12	62	2.71	27	2.69	4	0	2
13	22	2.54	18	2.54	6	0	1
14	51	2.09	43	2.09	4	0	4
15	29	2.06	29	2.06	6	0	2
16	25	1.99	19	1.98	5	1	3
17	48	1.89	42	1.89	0	2	0
18	25	1.74	15	1.74	5	1	4
19	12	1.65	11	1.65	7	1	2
20	47	1.59	26	1.59	2	2	3
21	21	1.56	20	1.55	7	1	4
22	24	1.54	21	1.55	4	2	2
23	15	1.53	9	1.53	4	0	5
24	10	1.52	13	1.52	6	2	1
25	17	1.51	8	1.51	10	0	2
26	15	1.50	5	1.50	0	0	6
27	23	1.48	8	1.48	9	1	1
28	15	1.41	9	1.41	1	1	6
29	61	1.40	20	1.40	4	2	4

Crystal structure

A complete crystal structure refinement could not be carried out due to the micro-crystalline nature of the sample (see Fig. 2); the diffraction patterns are neither single-crystal nor powder, and contain multiple phases, along with being mounted on a glass slide. In light of the limited nature of the data (not powder, not single-crystal, and not a lot of observables), a high-quality Rietveld refinement of the proportions of the different phases was not realistic. The best approach was, therefore, to average all seven background-corrected diffraction patterns and remove the peaks from the other phases. Whereas the peak intensities were not well constrained for Rietveld refinement, the peak positions produced reliable unit-cell parameters and confirmed the structural identity of this material.

It was not possible to refine the atomic coordinates of the oxygen atoms, as unrestricted refinement yielded inappropriate interatomic distances; however, refinement of the (Na,K) position, and the three Ti positions yielded atomic coordinates that compare favorably with the models of Andersson and Wadsley (1962) for $Na_2Ti_6O_{13}$, and Cid-Dresdner and Buerger (1962) for $K_2Ti_6O_{13}$. In the refinement of the data for nixonite, the occupancy of the Na1 site was fixed to Na 0.666, K 0.334, based on the EPMA data.

Nixonite is isostructural with jeppeite, ideally $K_2Ti_6O_{13}$, and consists of three chains of distorted, edge-sharing Ti-centered octahedra that extend along the *c*-axis. Two of the chains are connected by sharing corners along the *b*-axis, and the third chain links the first two by sharing edges with both. In this way, the structure can also be thought of as a zigzag chain of three Ti-centered octahedra edge-sharing along *b*. The alkali cations fit into tunnels formed by the Ti-octahedral framework, lying in a distorted cube coordination with eight oxygen atoms. (Fig. 6). The axes of the Ti-centered octahedra are parallel to the twofold *b*-axis (Fig. 6d).

Vibrational spectroscopy

The micro-Raman spectra collected on nixonite are shown in Figure 7 (black), where they are compared to the spectrum of $Na_2Ti_6O_{13}$ (red), synthesized at 800 to 1200 °C by Bamberger and Begun (1987). We did not observe any Raman peaks above 1000 cm^{-1} (see Supplemental[1] Material). The five main peaks of nixonite, in order of decreasing intensity, are (in cm^{-1}): 863, 280, 664, 135, and 113. Lower intensity peaks are evident in the 171–250 cm^{-1} and 332–618 cm^{-1} regions; two more peaks are centered at 97 and 747 cm^{-1}. The list of Raman peaks and their assignments are given in Supplemental[1] Table S1. The laser-stimulated fluorescence spectrum collected on nixonite is reported in Figure 8. The gap in the signal at around 900 nm of Figure 8 is due to double-diffraction from the 458 nm notch filter. The peaks observed between 450 and 500 nm in Figure 8 are Raman peaks and used to confirm that the fluorescence spectra are associated with nixonite.

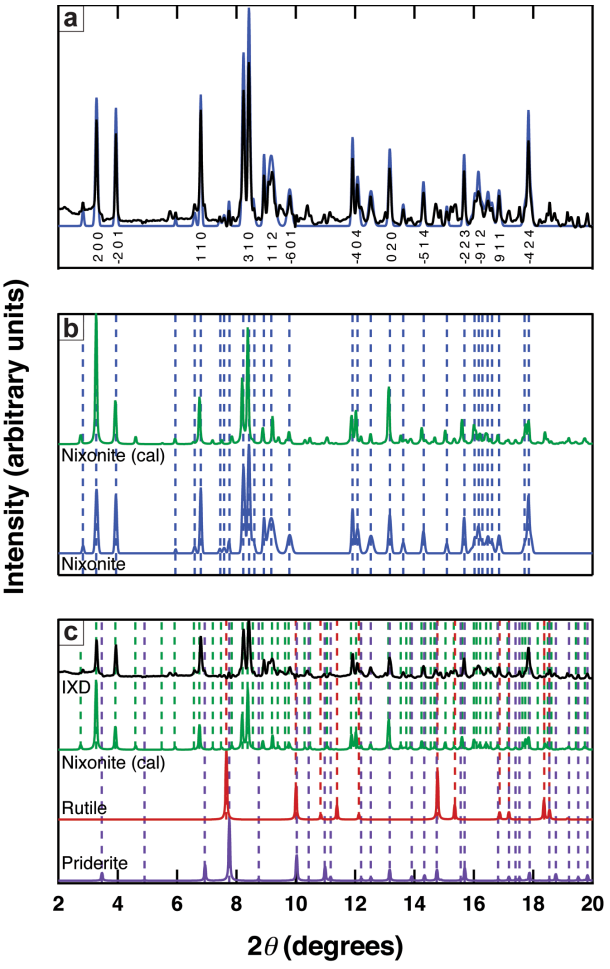

Figure 5. (**a**) The average of seven nixonite diffraction patterns after background correction is shown in black, while the blue pattern is the sum of all peaks that could be indexed as nixonite. This diffraction pattern was used to refine the unit-cell parameters of nixonite reported in the text. (**b**) Comparison between calculated nixonite diffraction pattern (green) and the sum of all peaks that could be indexed as nixonite (blue). The calculated diffraction pattern was produced by refining the lattice parameters from the masked diffraction pattern and a starting structure revised from synthetic $Na_2Ti_6O_{13}$ (space group *C*2/*m*). (**c**) Comparison between the calculated nixonite pattern (green), the average of DB1–DB7 after applying background correction (black) and the reference patterns of rutile: calculated from PowderCell (Kraus and Nolze 1996) using the structure from Swope et al. (1995), in red; and of priderite: calculated from PowderCell using the structure from Post et al. (1982), in purple. All of the peaks can be indexed by nixonite, rutile, and priderite. (Color online.)

Discussion

Occurrence and paragenesis

Nixonite occurs within a heavily metasomatized pyroxenite xenolith (~1 × 1 × 0.5 cm, Supplemental[1] Fig. S1) from the Darby kimberlite field, located ~200 km southwest of the community of Kugaaruk, Nunavut, Canada, beneath the west-central Rae Craton (67°23′56.6″N 93°21′13.9″W). This xenolith contains rutile, TiO_2, up to 200 μm in size, with a complex and thin reaction rim that consists of priderite, perovskite, freudenbergite, ilmenite, and nixonite (Fig. 1). Jeppeite was not recorded in the same reaction rim on rutile as nixonite, but was found in other thin sections from the same xenolith (Harris et al. 2018). Rutile is observed in various mantle xenocrysts and xenoliths but is most commonly found in eclogitic (Smith and Dawson 1975; Carswell 1990; Sobolev et al. 1997; Sobolev and Yefimova 2000) or mantle-metasomatic assemblages (e.g., MARID associations; Dawson and Smith 1977; Haggerty 1991). Priderite, freudenbergite, and jeppeite have been observed in a range of metasomatized mantle material (Jones et al. 1982; Mitchell and Lewis 1983; Haggerty et al. 1994; Giuliani et al. 2012). Jeppeite has been previously reported most commonly in lamproites, as a late-crystallizing groundmass phase (Pryce et al. 1984; Grey et al. 1998; Jaques 2016).

Relationship to other species

Nixonite can be compared to its K-analog, jeppeite, and to the only other known natural sodium–titanium oxides: freudenbergite and kudryavtsevaite.

Nixonite has the same structure as jeppeite, synthetic $Na_2Ti_6O_{13}$, and synthetic $K_2Ti_6O_{13}$. However, jeppeite and its synthetic analog $K_2Ti_6O_{13}$ have slightly larger unit-cell volumes, whereas synthetic $Na_2Ti_6O_{13}$ has a slightly smaller unit-cell volume. As one would expect among structural analogs, the positions of their main diffraction peaks are similar, whereas their intensities are different (Supplemental[1] Table S2).

Freudenbergite and kudryavtsevaite are the only other known natural sodium–titanium oxides (Ishiguro et al. 1978; Anashkin et al. 2013). Freudenbergite has the same space group as nixonite, but its unit-cell parameters are significantly different, as are the positions of its main diffraction peaks, with the exception of the main peak (located at 3.63 Å), which is close to the second-most intense peak of nixonite (located at 3.66 Å, Supplemental[1] Table S2). Kudryavtsevaite, in contrast, is orthorhombic and has a much larger unit-cell volume and very different diffraction peak-positions than nixonite; these two minerals can, therefore, be distinguished without ambiguity.

Implications

The first natural occurrence of nixonite is observed here to coexist within a single assemblage of freudenbergite, perovskite,

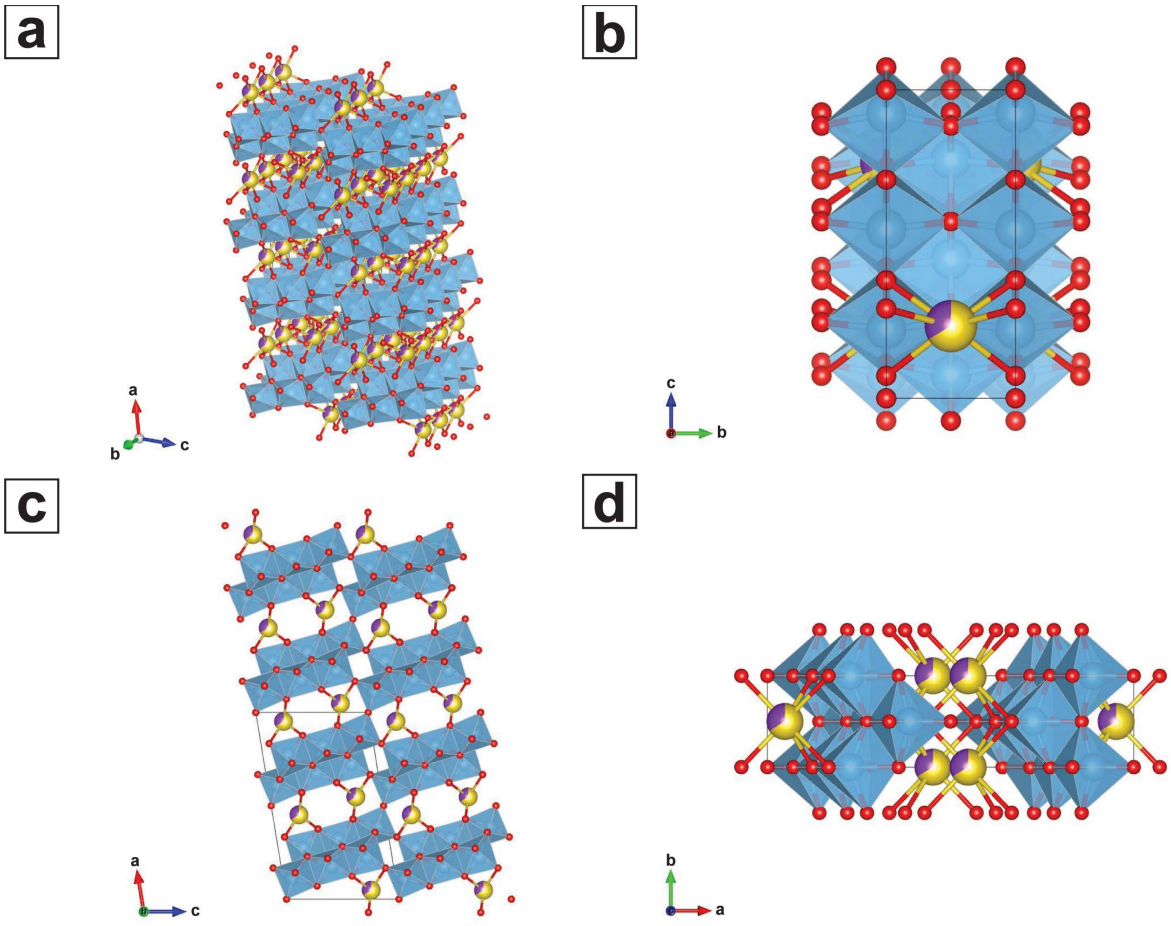

FIGURE 6. Crystal structure of nixonite (**a**) viewed obliquely down the *b* axis, showing the corrugated chains of (3-wide) edge-shared octahedra that extend along the *b* axis. (**b**) Viewed along the *a* axis. (**c**) Viewed along the *b* axis. (**d**) Viewed along the *c* axis. Oxygen atoms are represented in red, titanium-centered octahedra in blue, and sodium and potassium in yellow and purple, respectively. In **d**, it is evident that chains of Ti-centered octahedra are parallel to the *b* axis. (Color online.)

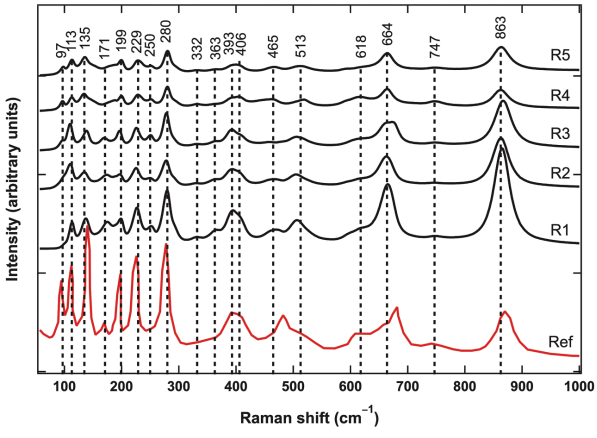

FIGURE 7. Raman spectra of nixonite (black) at five different positions labeled R1–R5 in Figure 1, and the spectrum of $Na_2Ti_6O_{13}$ (red), synthesized at 800 to 1200 °C by Bamberger and Begun (1987). (Color online.)

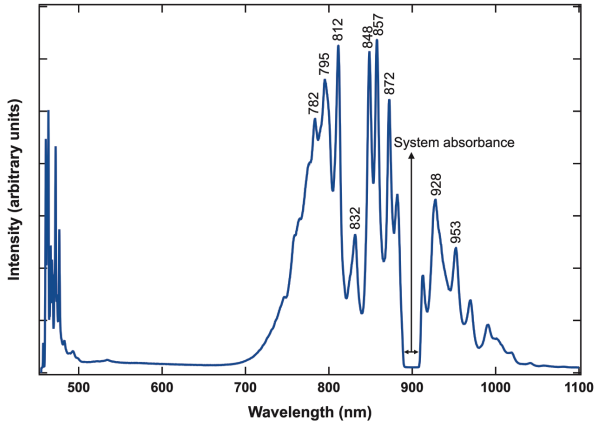

FIGURE 8. Fluorescence spectrum of nixonite acquired at position R2 (Fig. 1), excited by the 458 nm laser used for Raman spectroscopy. The extinction of light at around 900 nm is due to second-order diffraction by the 458 nm holographic notch filter and is thus an artifact of the spectroscopic system. The observed peaks below 500 nm correspond to Raman scattering. (Color online.)

and priderite within a pyroxenite xenolith from the Darby kimberlite field. These other minerals, together with jeppeite, are also found in six mantle-derived garnet pyroxenites within a metasomatic mineral suite that surrounds rutile grains and/or occurs as discrete grains in the case of jeppeite (Harris et al. 2018).

Freudenbergite and priderite have been previously reported in metasomatized peridotites sampled by kimberlites from southern Africa and North America (Jones et al. 1982; Mitchell and Lewis 1983; Haggerty et al. 1994; Giuliani et al. 2012). Jeppeite is most commonly found as a late-crystallizing groundmass phase in lamproites (Haggerty 1987) but has also been recorded in metasomatized mantle peridotites within the Prarie Creek lamproite (Mitchell and Lewis 1983). Jeppeite has also been noted as a reaction rim on priderite (Mitchell and Bergman 1991). Hence, these K-Ba-Ti-rich metasomatic phases characteristically form in highly alkaline, relatively Ti-rich melts such as the groundmass of lamproites. The occurrence of jeppeite and nixonite in the reaction rims around rutile grains in the Darby pyroxenite xenolith seem to be mutually exclusive though there is a ready source of Ti, in addition to any input from the metasomatic melt. The lack of association of nixonite and jeppeite is consistent with their formation in different chemical environments: jeppeite (and priderite) form in ultrapotassic environments from fluids rich in K, Ba, and Ti (very high K/Na), whereas nixonite and freudenbergite appear to form in Na-rich, Ba-poor environments. Despite extensive searching, nixonite was not observed in any of the other numerous jeppeite occurrences around rutile grains within this pyroxenite, whereas jeppeite is absent from the assemblage containing nixonite. This may reflect small-scale variations in the relative K and Na contents of the metasomatic melt or different stages in the evolution of the metasomatic melt. Freudenbergite, a Na-rich mineral, only occurs in the reaction rim containing nixonite in this rock, with whatever K was present being accommodated by priderite in this assemblage. The textural relationships between nixonite and priderite around the rutile in sample M-2B-3A are complex (Fig. 1), in places directly mantling rutile and in other places mantling priderite. Without other grains from which to constrain these relations, we cannot rule out the role of sectioning effects in creating these spatial relationships.

Among the nine bodies that constitute the Darby kimberlite field, most are classified as archetypal (or Group-I) kimberlites, but one is reported to be of "lamprophyre" affinity based on initial diamond exploration studies. Moreover, Sarkar et al. (2018) have recently reported the occurrence of intrusive rocks at Aviat, to the east of the Darby field, that are akin to orangeites (previously also known as Group-II kimberlites), which have close mineralogical and compositional similarities to lamproites. The occurrences of freudenbergite and the crichtonite-magnetoplumbite series minerals in metasomatized peridotites derived from kimberlites of the Kimberley area, South Africa, is notable because the K-Ba-Ti-rich MARID-like metasomatism there has been proposed to be the source of orangeites (Giuliani et al. 2015). Such K-Ti mantle metasomatism also was invoked for the formation of yimengite reaction rims around xenocrystic spinel in Venezuelan kimberlites, by Nixon and Condliffe (1989).

A mantle origin for the garnet pyroxenites containing nixonite and jeppeite was established using the approach of Hardman et al. (2018). Hence, the complex Na-K-Ti rich metasomatic mineral assemblages recorded beneath the Darby kimberlite field could reflect traces of an unusual metasomatic melt that percolated into the lithospheric mantle. Giuliani et al. (2012) have suggested that such complex titanium oxides, also found with alkali salts within Kimberley mantle xenoliths, originate from alkali-carbonate melts that percolate through cratonic lithospheric mantle.

There are other alternatives to consider. The Darby kimberlites and their host peridotites and eclogites have been subject to intense later-stage serpentinization (Harris et al. 2018). However, there are no records of the Na-K-Ti rich assemblage reported here being related to late stage alteration in the crust. This, and the lack of these assemblages around rutile in other Darby pyroxenites that are similarly altered/serpentinized, gives us confidence that the nixonite and other minerals in the rutile reaction rim of sample M-2B-3A did not form as a result of low-temperature alteration. Nonetheless, this does not preclude metasomatic alteration taking place during magma infiltration into the pyroxenite, in the course of kimberlite sampling, transport, and crystallization. This option is very difficult to differentiate from metasomatism of the pyroxenite by passing metasomatic melts while the pyroxenite was still residing in the mantle lithosphere beneath the Darby kimberlite field, prior to kimberlite sampling, because of the lack of determined phase relations for jeppeite and nixonite at geologically meaningful conditions. Transport by the host kimberlite and the subsequent evolution of an alkali-rich melt during kimberlite crystallization, as documented by Giuliani et al. (2017), producing a Na-rich melt could have invaded the pyroxenite and caused alteration of the rutile. This melt infiltration could have been responsible for the generation of the complex assemblage of Na-K-Ti rich minerals observed here, with Ti being derived from the pre-existing rutile.

The late groundmass crystallization of jeppeite in lamproites, together with its previously observed reaction-relationship with priderite, has been used to infer a low-pressure origin for this mineral (Chakhmouradian and Mitchell 2001). By inference, a low-pressure origin for nixonite, via reaction with an evolved kimberlitic melt seems as, or more, likely than a mantle metasomatic origin, until the stability relations of the jeppeite–nixonite series are determined.

Acknowledgments

We thank Gerhard Brey, A.L. Jaques, and an anonymous reviewer for suggestions that led to the improvement of the manuscript, and Paolo Lotti for careful editorial handling.

Funding

This research was financially supported by a Canada Excellence Research Chair (CERC) grant to D.G.P., and by the Diamond Exploration and Research Training School (DERTS), both funded by NSERC. S.D.J. acknowledges support from the U.S. National Science Foundation (NSF) EAR-1853521. We acknowledge Teck Resources Limited for granting access to the Darby property and support with field costs. Mike Merante provided invaluable assistance in the field. Work performed at GSECARS (sector 13) of the Advanced Photon Source (APS) is supported by the NSF EAR-1634415 and the Department of Energy (DOE) DEFG02-94ER1446. The APS is operated for the DOE Office of Science by Argonne National Laboratory under Contract No. DE-AC02-06CH11357. Experiments at Sector 13-BM-C of the APS used the PX2 facility, supported by COMPRES under NSF Cooperative Agreement EAR-1661511.

References cited

Anashkin, S., Bovkun, A., Bindi, L., Garanin, V., and Litvin, Y. (2013) Kudryavtsevaite, $Na_3MgFe^{3+}Ti_4O_{12}$, a new kimberlitic mineral. Mineralogical Magazine,

77, 327–334.
Andersson, S., and Wadsley, A.D. (1962) The structures of $Na_2Ti_6O_{13}$ and $Rb_2Ti_6O_{13}$ and the alkali metal titanates. Acta Crystallographica, 15, 194–201.
Bamberger, C.E., and Begun, G.M. (1987) Sodium titanates: stoichiometry and Raman spectra. Journal of the American Ceramic Society, 70, C-48–C-51.
Carswell, D.A. (1990) Eclogite and eclogite facies: definitions and classification. In D.A. Carswell, Ed., Eclogite Facies Rocks, p. 1–13. Blackie, New York.
Cech, O., Castkova, K., Chladil, L., Dohnal, P., Cudek, P., Libich, J., and Vanysek, P. (2017) Synthesis and characterization of $Na_2Ti_6O_{13}$ and $Na_2Ti_6O_{13}/Na_2Ti_3O_7$ sodium titanates with nanorod-like structure as negative electrode materials for sodium-ion batteries. Journal of Energy Storage, 14, 391–398.
Chakhmouradian, A., and Mitchell, R.G. (2001) Crystal structure of novel high-pressure perovskite $K_{2/3}Th_{1/3}TiO_3$, a possible host for Th in the upper mantle. American Mineralogist, 86, 1076–1080.
Cid-Dresdner, H., and Buerger, M.J. (1962) The crystal structure of potassium hexatitanate $K_2Ti_6O_{13}$. Zeitschrift für Kristallographie—Crystalline Materials, 117, 411–430.
Dawson, J.B., and Smith, J.V. (1977) The MARID (mica-amphibole-rutile-ilmenite-diopside) suite of xenoliths in kimberlite. Geochimica et Cosmochimica Acta, 41, 309–323.
Donovan, J.J., Kremser, D., Fournelle, J.H., and Goemann, K. (2015) Probe for EPMA: Acquisition, automation and analysis, version 11: Eugene, Oregon, Probe Software, Inc. http://www.probesoftware.com.
Giuliani, A., Kamenetsky, V.S., Phillips, D., Kendrick, M.A., Wyatt, B.A., and Goemann, K. (2012) Nature of alkali-carbonate fluids in the sub-continental lithospheric mantle. Geology, 40, 967–970.
Giuliani, A., Phillips, D., Woodhead, J.D., Kamenetsky, V.S., Fiorentini, M.L., Maas, R., Soltys, A., and Armstrong, R.A. (2015) Did diamond-bearing orangeites originate from MARID-veined peridotites in the lithospheric mantle? Nature Communications, 6, 6837, 10 p.
Giuliani, A., Soltys, A., Phillips, D., Kamenetsky, V.S., Maas, R., Goemann, K., Woodhead, J. Drysdale, R., and Griffin, W.L. (2017) The final stages of kimberlite petrogenesis: Petrography, mineral chemistry, melt inclusions and Sr-C-O isotope geochemistry of the Bultfontein kimberlite (Kimberley, South Africa). Chemical Geology, 455, 342–356.
Grey, I.E., Velde, D., and Criddle, A.J. (1998) Haggertyite, a new magnetoplumbite-type titanate mineral from the Prairie Creek (Arkansas) lamproite. American Mineralogist, 83, 1323–1329.
Haggerty, S.E. (1987) Metasomatic mineral titanates in upper mantle xenoliths. In P.H. Nixon, Ed., Mantle Xenoliths, p. 671–690. Wiley.
——— (1991) Oxide minerals: petrological and magnetic significance. Reviews in Mineralogy, 25, 355–416.
Haggerty, S.E., Fung, A.T., and Burt, D.M. (1994) Apatite, phosphorus and titanium in eclogitic garnet from the upper mantle. Geophysical Research Letters, 21, 1699–1702.
Hardman, M.F., Pearson, D.G., Stachel, T., and Sweeney, R.J. (2018) Statistical approaches to the discrimination of crust-and mantle-derived low-Cr garnet–Major-element-based methods and their application in diamond exploration. Journal of Geochemical Exploration, 186, 24–35.
Harris, G.A., Pearson, D.G., Liu, J., Hardman, M.F., Snyder, D.B., and Kelsch, D. (2018) Mantle composition, age and geotherm beneath the Darby kimberlite field, West Central Rae craton. Mineralogy and Petrology, 112, 57–70.
Holland, T.J.B., and Redfern, S.A.T. (1997) Unit cell refinement from powder diffraction data: the use of regression diagnostics. Mineralogical Magazine, 61, 65–77.
Ishiguro, T., Tanaka, K., Marumo, F., Ismail, M.G.M.U., Hirano, S., and Sōmiya, S. (1978) Freudenbergite. Acta Crystallographica, B34, 255–256.
Jaques, A.L. (2016) Major and trace element variations in oxide and titanate minerals in the West Kimberley lamproites, Western Australia. Mineralogy and Petrology, 110, 159–197.
Jones, A.P., Smith, J.V., and Dawson, J.B. (1982) Mantle metasomatism in 14 veined peridotites from Bultfontein Mine, South Africa. Journal of Geology, 90, 435–453.
Kolen'ko, Y.V., Kovnir, K.A., Gavrilov, A.I., Garshev, A.V., Frantti, J., Lebedev, O.I., Churagulov, B.R., Van Tendeloo, G., and Yoshimura, M. (2006) Hydrothermal synthesis and characterization of nanorods of various titanates and titanium dioxide. Journal of Physical Chemistry B, 110, 4030–4038.
Kraus, W., and Nolze, G. (1996) POWDER CELL—a program for the representation and manipulation of crystal structures and calculation of the resulting X-ray powder patterns. Journal of Applied Crystallography, 29, 301–303.
Liu, H., Yang, D., Zheng, Z., Ke, X., Waclawik, E., Zhu, H., and Frost, R.L. (2010) A Raman spectroscopic and TEM study on the structural evolution of $Na_2Ti_3O_7$ during the transition to $Na_2Ti_6O_{13}$. Journal of Raman Spectroscopy, 41, 1331–1337.
Mandarino, J.A. (1979) The Gladstone-Dale relationship; Part III, Some general applications. Canadian Mineralogist, 17, 71–76.
——— (1981) The Gladstone-Dale relationship; Part IV, The compatibility concept and its application. Canadian Mineralogist, 19, 441–450.
Mitchell, R.H., and Bergman, S.C. (1991) Petrology of Lamproites, 447 p. Plenum Press, New York.
Mitchell, R.H., and Lewis, R.D. (1983) Priderite-bearing xenoliths from the Prairie Creek mica peridotite, Arkansas. Canadian Mineralogist, 21, 59–64.
Nixon, P.H., and Condliffe, E. (1989) Yimengite of K-Ti metasomatic origin in kimberlitic rocks from Venezuela. Mineralogical Magazine, 53, 305–309.
Nixon, P.H., and Hornung, G. (1968) A new chromium garnet end member, knorringite, from kimberlite. American Mineralogist, 53, 1833–1840.
Pearson, D.G., Davies, G.R., Nixon, P.H., and Milledge, H.J. (1989) Graphitized diamonds from a peridotite massif in Morocco and implications for anomalous diamond occurrences. Nature, 338, 60–62.
Post, J.E., Von Dreele, R.B., and Buseck, P.R. (1982) Symmetry and cation displacements in hollandites: structure refinements of hollandite, cryptomelane and priderite. Acta Crystallographica, B38, 1056–1065.
Prescher, C., and Prakapenka, V.B. (2015) DIOPTAS: a program for reduction of two-dimensional X-ray diffraction data and data exploration. High Pressure Research, 35, 223–230.
Pryce, M.W., Hodge, L.C., and Criddle, A.J. (1984) Jeppeite, a new K-Ba-Fe titanate from Walgidee Hills, Western Australia. Mineralogical Magazine, 48, 263–266.
Sarkar, C., Kjarsgaard, B.A., Pearson, D.G., Heaman, L.M., Locock, A.J., and Armstrong, J.P. (2018) Geochronology, classification, and mantle source characteristics of kimberlites and related rocks from the Rae Craton, Melville Peninsula, Nunavut, Canada. Mineralogy and Petrology, 112, 653–672.
Smith, J.V., and Dawson, J.B. (1975) Chemistry of Ti-poor spinels, ilmenites and rutiles from peridotite and eclogite xenoliths. Physics and Chemistry of the Earth, 309–322.
Sobolev, N.V., and Yefimova, E.S. (2000) Composition and petrogenesis of Ti-oxides associated with diamonds. International Geology Review, 42, 758–767.
Sobolev, N.V., Kaminsky, F.V., Griffin, W.L., Yefimova, E.S., Win, T.T., Ryan, C.G., and Botkunov, A.I. (1997) Mineral inclusions in diamonds from the Sputnik kimberlite pipe, Yakutia. Lithos, 39, 135–157.
Swope, R.J., Smyth, J.R., and Larson, A.C. (1995) H in rutile-type compounds: I. Single-crystal neutron and X-ray diffraction study of H in rutile. American Mineralogist, 80, 448–453.
Toby, B.H., and Von Dreele, R.B. (2013) GSAS-II: the genesis of a modern open-source all purpose crystallography software package. Journal of Applied Crystallography, 46, 544–549.
Zeng, Q.G., Yang, G.T., Chen, F., Luo, J.Y., Zhang, Z.M., Leung, C.W., Ding, Z.J., and Sheng, Y.Q. (2013) Pressure effect on the Raman and photoluminescence spectra of Eu^{3+}-doped $Na_2Ti_6O_{13}$ nanorods. High Pressure Research, 33, 734–744.
Zhang, D., Dera, P.K., Eng, P.J., Stubbs, J.E., Zhang, J.S., Prakapenka, V.B., and Rivers, M.L. (2017) High pressure single crystal diffraction at PX^2. Journal of Visualized Experiments: JoVE, 119, e54660. DOI: 10.3791/54660.
Zhu, K.R., Yuan, Y., Zhang, M.S., Hong, J.M., Deng, Y., and Yin, Z. (2007) Structural transformation from $NaHTi_3O_7$ nanotube to $Na_2Ti_6O_{13}$ nanorod. Solid State Communications, 144, 450–453.

Manuscript received February 25, 2019
Manuscript accepted May 17, 2019
Manuscript handled by Paolo Lotti

Endnote:

[1]Deposit item AM-19-97023, Supplemental Material. Deposit items are free to all readers and found on the MSA website, via the specific issue's Table of Contents (go to http://www.minsocam.org/MSA/AmMin/TOC/2019/Sep2019_data/Sep2019_data.html).